JCI insight

CD4⁺ T cells induce rejection of urothelial tumors after immune checkpoint blockade

Yuji Sato, … , Jennifer K. Sehn, Vivek K. Arora

JCI Insight. 2018;3(23):e121062. https://doi.org/10.1172/jci.insight.121062.

Research Article Immunology Oncology

Immune checkpoint blockade (ICB) provides clinical benefit to a minority of patients with urothelial carcinoma (UC). The role of CD4$^+$ T cells in ICB-induced antitumor activity is not well defined; however, CD4$^+$ T cells are speculated to play a supportive role in the development of CD8$^+$ T cells that kill tumor cells after recognition of tumor antigens presented by MHC class I. To investigate the mechanisms of ICB-induced activity against UC, we developed mouse organoid-based transplantable models that have histologic and genetic similarity to human bladder cancer. We found that ICB can induce tumor rejection and protective immunity with these systems in a manner dependent on CD4$^+$ T cells but not reliant on CD8$^+$ T cells. Evaluation of tumor infiltrates and draining lymph nodes after ICB revealed expansion of IFN-γ–producing CD4$^+$ T cells. Tumor cells in this system express MHC class I, MHC class II, and the IFN-γ receptor (Ifngr1), but none were necessary for ICB-induced tumor rejection. IFN-γ neutralization blocked ICB activity, and, in mice depleted of CD4$^+$ T cells, IFN-γ ectopically expressed in the tumor microenvironment was sufficient to inhibit growth of tumors in which the epithelial compartment lacked Ifngr1. Our findings suggest unappreciated CD4$^+$ T cell–dependent mechanisms of ICB activity, principally mediated through IFN-γ effects on the microenvironment.

Find the latest version:

https://jci.me/121062/pdf

JCI insight

RESEARCH ARTICLE

CD4⁺ T cells induce rejection of urothelial tumors after immune checkpoint blockade

Yuji Sato,[1] Jennifer K. Bolzenius,[1] Abdallah M. Eteleeb,[2] Xinming Su,[1] Christopher A. Maher,[1,2] Jennifer K. Sehn,[3] and Vivek K. Arora[1]

[1]Department of Internal Medicine, Division of Oncology, [2]McDonnell Genome Institute, and [3]Department of Pathology and Immunology, Washington University School of Medicine, St. Louis, Missouri, USA.

Immune checkpoint blockade (ICB) provides clinical benefit to a minority of patients with urothelial carcinoma (UC). The role of $CD4^+$ T cells in ICB-induced antitumor activity is not well defined; however, $CD4^+$ T cells are speculated to play a supportive role in the development of $CD8^+$ T cells that kill tumor cells after recognition of tumor antigens presented by MHC class I. To investigate the mechanisms of ICB-induced activity against UC, we developed mouse organoid-based transplantable models that have histologic and genetic similarity to human bladder cancer. We found that ICB can induce tumor rejection and protective immunity with these systems in a manner dependent on $CD4^+$ T cells but not reliant on $CD8^+$ T cells. Evaluation of tumor infiltrates and draining lymph nodes after ICB revealed expansion of IFN-γ–producing $CD4^+$ T cells. Tumor cells in this system express MHC class I, MHC class II, and the IFN-γ receptor (Ifngr1), but none were necessary for ICB-induced tumor rejection. IFN-γ neutralization blocked ICB activity, and, in mice depleted of $CD4^+$ T cells, IFN-γ ectopically expressed in the tumor microenvironment was sufficient to inhibit growth of tumors in which the epithelial compartment lacked Ifngr1. Our findings suggest unappreciated $CD4^+$ T cell–dependent mechanisms of ICB activity, principally mediated through IFN-γ effects on the microenvironment.

Conflict of interest: YS received salary from Shionogi & Co. Ltd. while working on this project.

License: Copyright 2018, American Society for Clinical Investigation.

Submitted: March 13, 2018
Accepted: October 31, 2018
Published: December 6, 2018

Reference information:
JCI Insight. 2018;3(23):e121062.
https://doi.org/10.1172/jci.insight.121062.

Introduction

Urothelial carcinoma (UC) arising in the urinary tract is the sixth most commonly diagnosed malignancy in the US. Standard therapy for localized UC includes intravesical Bacillus Calmette–Guérin (BCG) instillation, which induces antitumor activity via T cell–dependent mechanisms (1, 2). Systemic immunotherapy with immune checkpoint blockade (ICB) has now also demonstrated clear activity in approximately 15%–25% of patients with metastatic disease, often with impressive duration of response, leading the US Food and Drug Administration to approve 5 drugs targeting either PD-1 or PD-L1 for use in metastatic UC in the last 3 years (3–9). Phase III trials are testing these agents in combination with CTLA-4–targeting antibodies after earlier studies indicated combined treatment improves response rate to 39% (Clinicaltrials.gov, NCT01928394, NCT03036098, NCT02516241) (10). Unfortunately, combination treatment also increases toxicity, and only a minority of patients respond. The identification of predictive biomarkers for ICB response and the development of optimal combination regiments with immunotherapies thus remain among the most pressing unmet needs in UC clinical management.

While ICB is well documented to enhance T cell function, the precise mechanisms by which ICB induces bladder tumor killing remain poorly defined, hampering predictive biomarker discovery and the development of optimal combinations. Clinical trials using PD-1/PD-L1–targeting agents have evaluated the predictive value of PD-L1 staining on tumor cells and/or infiltrating immune cells by IHC, but cross trial comparisons are challenging due to a lack of standardization in staining methodologies and signal analysis (3–9). To date, staining for PD-L1 correlates with response in some but not all trials. Moreover, PD-L1 staining may be absent in patients who nonetheless respond. Currently, there is an absence of clear evidence supporting PD-L1 expression in the epithelial compartment of tumors as critical for ICB activity against UC. Since IFN-γ induces PD-L1 expression on epithelial cells as a physiologic homeostatic mechanism to dampen T cell responses, it is possible that the utility of PD-L1 expression as a biomarker may be related to the extent that it serves as a marker for IFN-γ activity within the tumor (11). In support of this, PD-L1 expression in bladder tumors correlated with an intratumoral IFN-γ activity gene signature (12), and in a separate clinical study, an IFN-γ activity signature correlated with bladder cancer response to the PD-1 inhibitor nivolumab (7). IFN-γ exerts pleiotropic effects in the tumor environment, including upregulation of MHC class I expression and antigen presentation in tumor cells (13). In addition to serving as a biomarker, IFN-γ activity may be mechanistically involved in ICB activity against UC, and indeed, IFN-γ–producing $CD4^+$ T cells have been documented to expand after neoadjvuant ICB treatment of bladder cancer patients (14, 15). While one role of these $CD4^+$ T cells in ICB-induced tumor immunity may be to support $CD8^+$ T cell–mediated killing, if there are other roles of IFN-γ and Th1-like $CD4^+$ T cells in ICB activity, they are not documented.

Preclinical studies of bladder cancer response to ICB have relied largely on MB49, a bladder cancer line derived from ex vivo carcinogenesis of bladder tissue (16). Shi et al. showed that the combination PD-1 and CTLA-4 blockade was more effective than single-agent therapy against s.c. MB49 tumors (17). Vandeveer et al. showed that αPD-L1 was active against orthotopically implanted MB49 tumors (18). In these studies, both $CD4^+$ and $CD8^+$ T cells appear to play a role in antitumor activity, consistent with a model in which they have interdependent function. An important caveat, however, is that MB49 underwent carcinogenesis ex vivo in the absence of immune surveillance and has been passaged in vitro over several decades. Thus, its antigenic profile, and by extension the nature of the T cell responses it elicits, may not accurately reflect tumors subjected to immune-mediated editing during oncogenesis and progression. Here, we document the generation of models of bladder cancer tumor immunity and characterize the mechanistic basis of their sensitivity to ICB with the goal of broadening our understanding of the effector mechanism by which ICB can induce antitumor activity.

Results

Generation and characterization of organoid-based transplantable UC models. Human urothelial cancer is strongly associated with exposure to mutagenic carcinogens, and overall mutation burden correlates with likelihood of response to ICB (3, 4). To develop an immunogenic transplantable mouse model with which to study immune effector mechanisms necessary for ICB activity, we induced bladder tumors in mice by exposure to the carcinogen 4-hydroxybutyl(butyl)nitrosamine (BBN) via drinking water for 22 weeks. With this approach, mice develop carcinoma in situ and areas of invasive UC, sometimes with areas of squamous differentiation (Figure 1A) (19). Using tissue from tumor-bearing bladder, we propagated transformed urothelium in an organoid culture system and then isolated clonal sublines (Figure 1A) (20). Clonal sublines MCB6A and MCB6C were identified as subclonal tumorigenic organoid lines that grow with predictable kinetics (Figure 2A and Supplemental Figure 1D; supplemental material available online with this article; https://doi.org/10.1172/jci.insight.121062DS1). In contrast, organoid cultures established from normal bladder failed to generate tumor masses after s.c. transplantation into syngeneic mice (Figure 2A, MCU24) (21), indicating that only transformed tissue can form tumors with this approach.

Analysis by TCGA of human UC has recognized 5 molecular subtypes based on expression profiles, with 35% percent of cases classified as "basal-squamous" (22). This subclass is characterized by the presence of more extensive immune infiltrates and better clinical responses compared with other subclasses (22, 23). MCB6A and MCB6C organoids generate urothelial tumors with features similar to the basal-squamous subtype, showing morphology reminiscent of human UC with squamous features. Moreover, tumor cells stained positive for cytokeratin 5 (Ck5), a marker of the basal-squamous tumors, and were negative for the luminal epithelial marker UPKIII (Figure 1B and Supplemental Figure 1A). The organoid tumors also recruited an organized appearing stromal compartment, with extensive SMA^+ fibroblasts and $CD31^+$ endothelial cells (Figure 1B). Mutation analysis of MCB6C identified 1,526 mutations, including probable driver mutations in orthologs of genes commonly mutated in human bladder cancer (see Table 1) (24). TP53 mutations are found in 28%–49% of human bladder cancers and tend to co-occur with mutations in the KDM6A tumor suppressor, a histone demethylase mutated in approximately 25% of cases. Activating RAS mutations have been reported in 5%–24% of cases (25, 26). MCB6A harbors 1,524 mutations and, similar to MCB6C, has mutations in Kdm6a and Trp53. However, the majority of mutations in MCB6A are unique compared with MCB6C (Supplemental Figure 1B). For example, MCB6A lacks a Kras mutation and harbors a candidate oncogenic mutation in Sf3b1, an RNA-splicing factor in which the orthologous mutation has been identified in human lung and bladder cancer specimens (Supplemental Figure 1C) (26). Thus, we have identified two organoids models with histologic and genetic features in common with human UC.

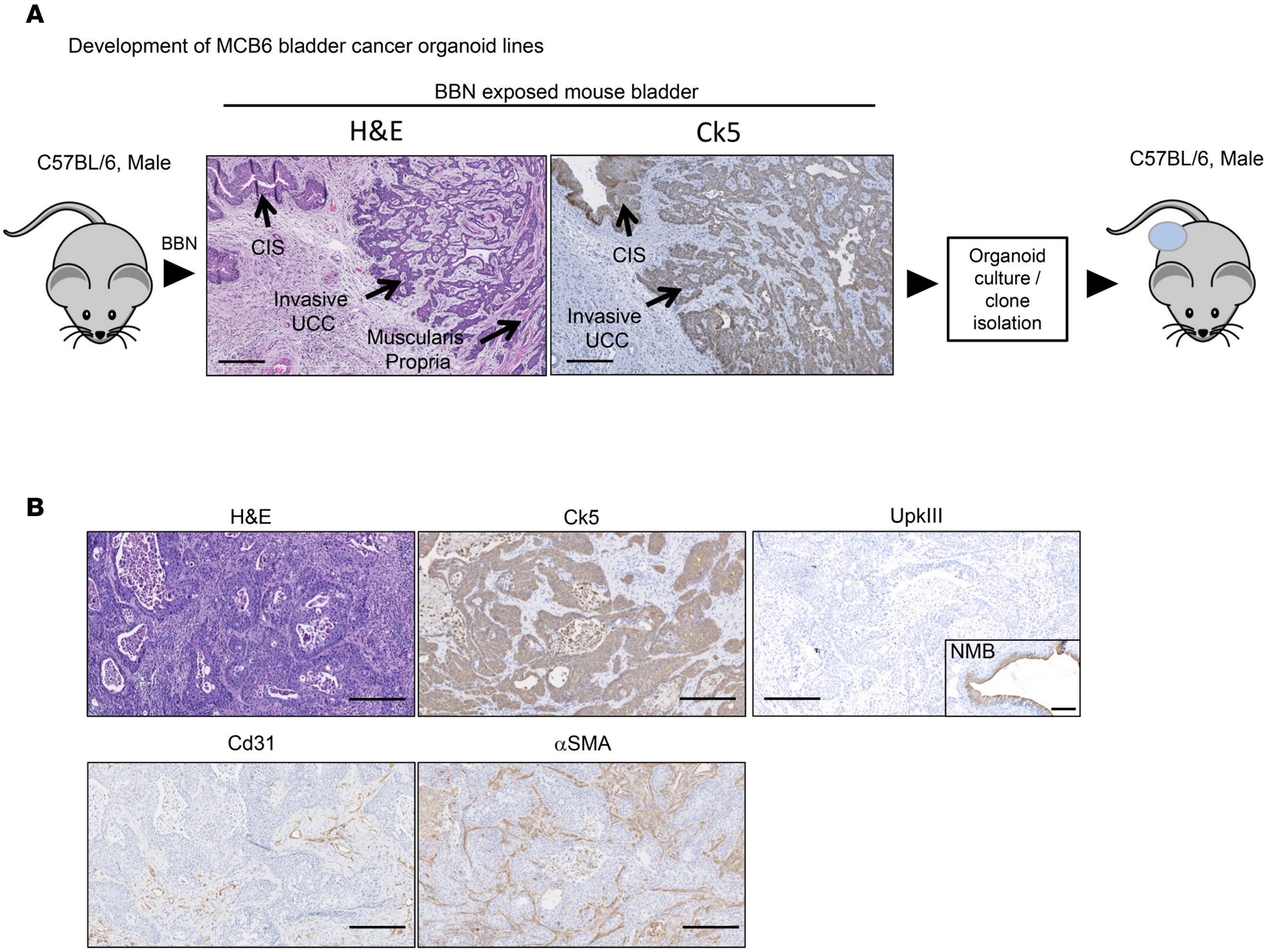
A
Development of MCB6 bladder cancer organoid lines
BBN exposed mouse bladder
H&E
Ck5
C57BL/6, Male
BBN
CIS
Invasive UCC
Muscularis Propria
CIS
Invasive UCC
Organoid culture / clone isolation
C57BL/6, Male
B
H&E
Ck5
UpkIII
NMB
Cd31
αSMA

Figure 1. MCB6C is a transplantable organoid model of urothelial carcinoma, with features of human basal-squamous urothelial carcinoma. (**A**) Schematic representation of how the MCB6 organoid lines were established from a BBN-treated mouse. Images (original magnification, ×10) were obtained with NanoZoomer-XR. Scale bar: 200 μM. (**B**) Histologic and immunohistochemical evaluation of a s.c. MCB6C tumor collected 28 days after injection of organoid cells. A normal mouse bladder (NMB) specimen was used as positive control for UPKIII staining. Scale bar: 200 μM.

Identification of immune cells that restrain organoid tumor growth and mediate ICB-induced rejection. To determine if organoid tumors are subject to T cell–mediated growth regulation, we measured the effect of antibody-mediated depletion of T cells starting 3 days prior to s.c. organoid implantation. Combined CD4$^+$ and CD8$^+$ T cell depletion significantly hastened growth of MCB6C. CD4$^+$ T cell depletion alone similarly increased growth, while CD8$^+$ T cell depletion alone had no effect in this system (Figure 2A). Thus, MCB6C tumor growth is partially restrained by a CD4$^+$ T cell–dependent mechanism, even in the absence of ICB. When testing MC6CA tumors, T cell depletion did not significantly hasten growth (Supplemental Figure 1D). Successful T cell depletion in tumor-infiltrating lymphocytes (TILs) and peripheral blood was confirmed in identically treated mice by flow cytometry on day 28 (Supplemental Figure 2A). These findings suggest variability in the baseline immunogenicity of the two organoid lines.

We next determined the sensitivity of organoid tumors to ICB. First, MCB6C tumors were established in syngeneic mice, and 9 days after s.c. organoid implantation, mice were treated with αPD-1, αCTLA-4, or the combination (Figure 2B). Treatments were repeated every 3 days between days 9 and 24. αPD-1 or αCTLA-4 monotherapy induced antitumor activity and rejected tumors in 5 of 15 and 9 of 15 mice, respectively. Combination therapy was significantly more effective and caused tumor rejection in 14 of 15 tumor-bearing mice. To identify effector cells important for ICB-induced MCB6C tumor rejection, we depleted CD4$^+$ cells, CD8$^+$ cells, and NK cells starting on day 7, 2 days before initiation of ICB treatment. CD4$^+$ T cell depletion completely blocked combination ICB activity, while CD8$^+$ T cell depletion and NK cell depletion had not effect (Figure 2C). Because PD-1 blockade is more dependent on CD8$^+$ T cell

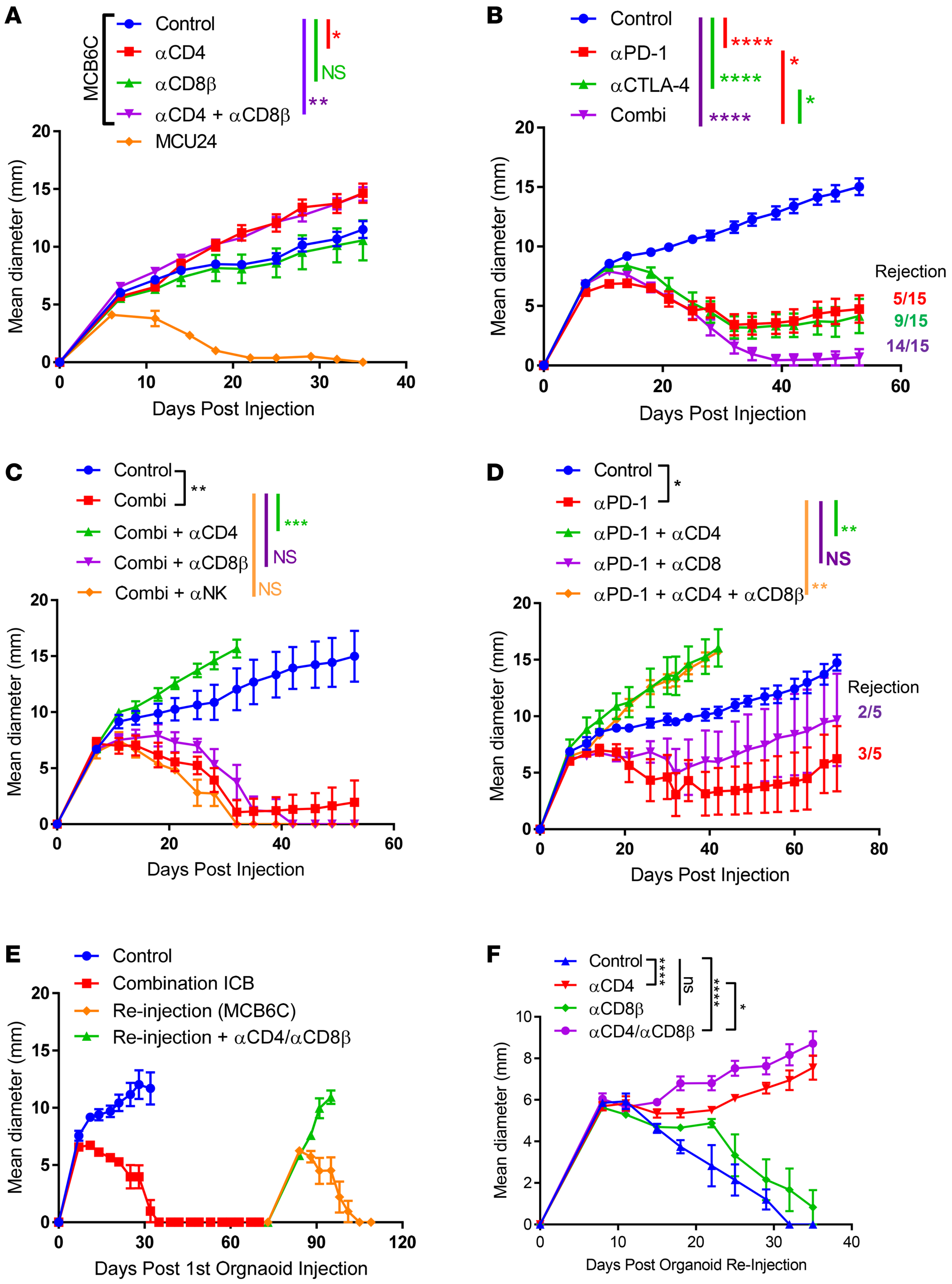

Figure 2. CD4⁺ T cells restrain growth of MCB6C and mediate ICB-induced tumor immunity. (**A**) In vivo CD4⁺ and/or CD8⁺ T cell depletion in MCB6C tumor-bearing mice. Each depletion antibody was injected i.p. starting 3 days before organoid injection and continued weekly. MCU24 is a urothelial organoid established from a normal, age-matched mouse. Data are shown as mean ± SEM. *n* = 5 mice per group. (**B**) Immune checkpoint blockade in MCB6C tumor-bearing mice. Each treatment started 9 days after tumor injection and was repeated every 3 days for a total of 6 treatments. Data are shown as mean ± SEM. *n* = 15 mice per group aggregated from 3 independent experiments. (**C**) αPD-1 and αCTLA-4 combination treatment coadministered with depleting antibodies for CD4⁺ T cells, CD8⁺ T cells, or NK cells. Depletion antibodies were injected i.p. starting 7 days after tumor injection, and ICB was initiated 9 days after tumor injection. Data represent mean tumor diameter ± SEM. *n* = 5 mice per group. (**D**) αPD-1 coadministered with CD4⁺ T cell and/or CD8⁺ T cell depletion. Depletion antibodies were injected i.p. starting 7 days after tumor injection, and ICB was initiated 9 days after tumor injection. Data represent mean tumor diameter ± SEM. *n* = 5 mice per group. (**E**) MCB6C tumor-bearing mice were treated with combination ICB as above. Mice in which the original tumor had been completely rejected were reinjected with MCB6C on day 73 with or without weekly combined CD4⁺ T cell and CD8⁺ T cell depletion. Data are plotted as mean diameter ± SEM of *n* = 5 mice per reinjection group. (**F**) Similar to **E**, but with individual depletion of CD4⁺ and CD8⁺ T cells. Data represent mean tumor diameter ± SEM. *n* = 5 mice per group. See also Supplemental Figure 2 for evaluation of depletion efficiency. All statistical comparisons by 2-way ANOVA for repeated measures. NS > 0.05, *$P < 0.05$, **$P < 0.01$, ***$P < 0.001$, ****$P < 0.0001$.

Table 1. Probable driver mutations identified in MCB6C and their human orthologs

Mouse	Human	Evidence for functional relevance
Trp53	TP53	Recurrent in human cancer (26)
T122K	T125K	
Kdm6a	KDM6A	Targets catalytic activity (24)
H1146Y	H1146Y	
Kras	KRAS	Recurrent in human cancer (26)
G12D	G12D	

function than CTLA-4 blockade in other cancer models, we repeated lymphocyte depletion experiments with PD-1 blockade alone using the MCB6C model (27). Again CD4$^+$ T cell depletion completely blocked antitumor activity, while CD8$^+$ T cell depletion did not have a significant effect (Figure 2D). To establish the generality of these observations, we repeated a similar experiment using the MCB6A line. MCB6A was also found to be sensitive to combination ICB, which induced rejection of 10 of 12 tumors (Supplemental Figure 1E). Again, CD4$^+$ T cell depletion completely blocked the activity of ICB, while CD8$^+$ T cell depletion did not significantly affect activity, affirming CD4$^+$ T cells as the key effector population for ICB activity against another organoid line (Supplemental Figure 1E). In all experiments, depletion of T cells was confirmed by flow cytometry (Supplemental Figure 1F and Supplemental Figure 2, B and C). These findings demonstrate that combination ICB or αPD1 can induce CD4$^+$ T cell–dependent antitumor immunity through a mechanism not affected by CD8$^+$ T cell depletion.

We next determined if ICB induced tumor rejection leads to the generation of protective T cell memory immunity. Mice bearing MCB6C tumors were treated with ICB starting on day 9, leading to tumor rejection. Starting on day 73, 7 weeks after the last ICB treatment and after rejection of all tumors, mice were then reinjected with MCB6C organoids, with and without combined depletion of CD4$^+$ and CD8$^+$ T cells starting 3 days prior to reinjection. In the absence of T cell depletion, the tumors spontaneously rejected, while T cell depletion enabled robust growth (Figure 2E). We then repeated a similar experiment, but this time individually depleted CD4$^+$ or CD8$^+$ T cells prior to rechallenge with MCB6C. CD4$^+$ T cell depletion enabled tumor growth of all 5 tumors, while 4 of 5 tumors were rejected despite CD8$^+$ T cell depletion. CD8$^+$ T cell depletion alone did not significantly impair tumor rejection but, when combined with CD4$^+$ depletion, modestly augmented growth of tumors compared with CD4$^+$ T cell depletion alone (Figure 2F). Successful T cell depletion was confirmed on day 28 after tumor reinjection by flow cytometry (Supplemental Figure 2D). These data suggest that CD8$^+$ T cells may also play a small and nonessential role in memory immune responses. In contrast, CD4$^+$ T cells are essential for an effective ICB-induced memory response against tumor rechallenge.

Characterization of ICB-induced changes in lymphocyte populations. To gain insight into the mechanism of antitumor activity, we next characterized the effects of ICB on TILs. We first focused on combination ICB, since it gave the most consistent antitumor activity. Mice bearing MCB6C tumors were treated with combination ICB on days 9 and 12 after organoid implantation. Tumors were then harvested on day 14 and evaluated by flow cytometry (Supplemental Figure 3). Total CD4$^+$ T cells, CD8$^+$ T cells, and NK cells were plotted as a percentage of total lymphocytes (Figure 3A). Compared with control, combination therapy led to robust intratumoral expansion of CD4$^+$ T cells but had only a modest, nonsignificant effect on the number of CD8$^+$ T cells. IHC analysis of tumors harvested at day 14 showed that, in the absence of ICB, CD4$^+$ T cells were primarily localized to stromal regions and after ICB they were pervasive throughout the inflammatory infiltrate (Supplemental Figure 4). CD8$^+$ T cells, in contrast, were located primarily within the epithelial compartment prior to ICB (Supplemental Figure 4).

We then evaluated the effect of ICB on the proportion of specific CD4$^+$ T cell subsets within the lymphocyte population, staining for T-bet, GATA3, RORγ, and FOXP3 as markers of Th1 cells, Th2 cells, Th17 cells, and Tregs, respectively (Figure 3B). In the tumor, only the T-bet$^+$ population was significantly changed by combination therapy. The T-bet$^+$/Foxp3$^+$CD4$^+$ T cell ratio significantly increased, but we did not observe absolute Treg depletion (Figure 3B). Since IFN-γ is a primary effector molecule produced by Th1 CD4$^+$ T cells, we also determined if combination ICB expands the number of IFN-γ–producing

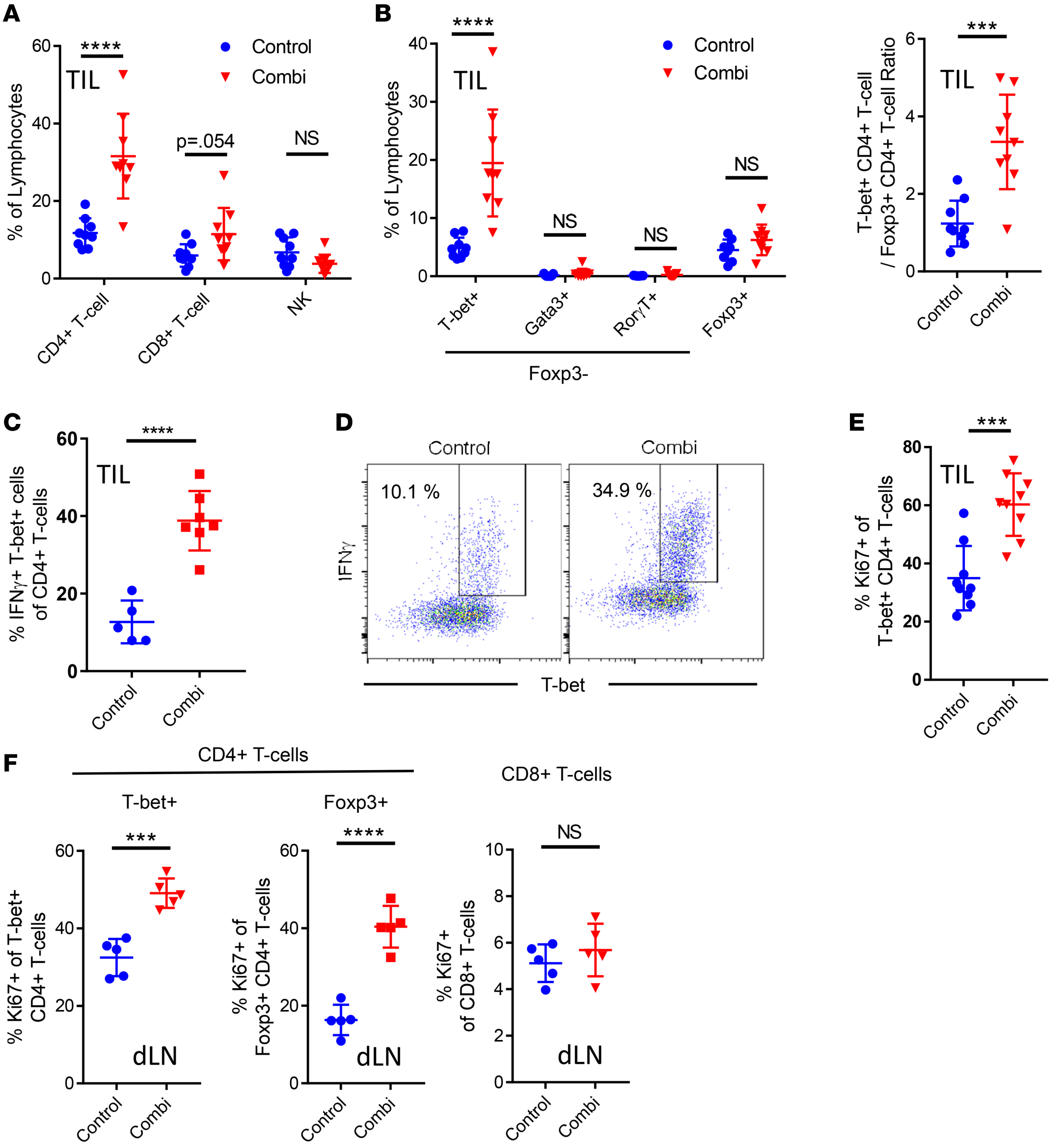

Figure 3. Immune checkpoint blockade induces expansion of Th1 CD4⁺ T cells that express T-bet and IFN-γ. (**A**) Tumor-infiltrating lymphocytes (TILs) were analyzed in day 14 tumors by flow cytometry. ICB was initiated on day 9 and repeated on day 12. Data are shown as mean ± SD from *n* = 9 tumors aggregated from 2 experiments. (**B**) CD4⁺ T cell subtype analysis in TILs by flow cytometry. ICB was initiated on day 9 and repeated on day 12. Data are shown as mean ± SD from *n* = 9 tumors aggregated from 2 experiments. (**C**) IFN-γ expression in intratumoral T-bet⁺CD4⁺ T cells after 4 hours of PMA/ionomycin stimulation in vitro. Data are plotted as mean ± SD from *n* = 5–8 tumors. (**D**) CD4⁺ T cells treated as in **C** and costained for IFN-γ and T-bet. (**E**) Similar to **B**, showing the percentage of T-bet⁺CD4⁺ TILs that stained for Ki67. (**F**) Percentage of Ki67⁺ cells in CD4⁺ or CD8⁺ T cells in dLNs on day 14 (mean ± SD). *n* = 5 mice. Combination ICB given on day 9 and 12. See also Supplemental Figure 3 for schematic of gating strategies. All statistical analysis by Student's *t* test. NS > 0.05, ***$P < 0.001$, ****$P < 0.0001$.

T-bet⁺CD4⁺ T cells. Five days following initiation of ICB, tumor suspensions were stimulated with PMA and ionomycin in vitro for 4 hours, and intracellular IFN-γ production was then evaluated in T cells by flow cytometry. Compared with that in control tumors, the proportion of IFN-γ–producing T-bet⁺CD4⁺ T cells significantly expanded (Figure 3C), and IFN-γ production was essentially restricted to the T-bet⁺ population (Figure 3D). Finally, combination treatment significantly increased the proportion of T-bet⁺CD4⁺ T cells in the tumor that stained positive for Ki67 (Figure 3E), indicating that one cause of intratumoral expansion is increased proliferation in the tumor microenvironment.

We next used flow cytometry to evaluate changes in T cell populations in the draining lymph node (dLN) following combination ICB. Total CD4$^+$ T cells relative to all lymphocytes did not expand with ICB combination therapy (Supplemental Figure 5A). Total T-bet$^+$CD4$^+$ cells also did not change (Supplemental Figure 5B), but the proportion that stained positive for Ki67 strongly increased (Figure 3F). We then evaluated expression of CD44 and the lymph node–homing receptor CD62L, which are often used to distinguish naive, central memory, and effector memory T cells. The majority of T-bet$^+$CD4$^+$ T cells were CD62LCD44$^+$, displaying a typical effector memory phenotype (Supplemental Figure 5D). However, there was a proportion found to be CD62L$^+$CD44$^–$, indicating retention of features of naive T cells. Combination ICB caused a decrease in the proportion of T-bet$^+$ cells with naive features and an increase in the proportion that were CD62L$^–$CD44$^+$ (Supplemental Figure 5D). These data suggest that ICB increases the proliferation and differentiation of T-bet$^+$CD4$^+$ effector memory cells within the secondary lymphoid tissue. We did observe a significant expansion of total Tregs in the dLN (Supplemental Figure 5B) and an increase in the proportion that were Ki67$^+$ (Figure 3F). There was also a relative expansion of the Treg population with a CD62L$^–$CD44$^+$ phenotype (Supplemental Figure 5F). However, these changes in Tregs in the dLN were not associated with a quantitative effect on the number of Tregs in the TILs at the same time point (Figure 3B). There was no significant effect of ICB on CD8$^+$ T cells in the dLN, as assessed by total number, Ki67 staining, or maturation to an effector memory phenotype (Figure 3F, Supplemental Figure 5H, and data not shown).

Single-agent ICB generated less consistent antitumor activity than combination ICB against MCB6C (Figure 2B). This potentially confounds analysis of immune perturbations acutely after single-agent ICB treatment, since, at the time of immune analysis, there remained uncertainty as to the eventual tumor fate. Nonetheless, we evaluated changes in a subset of mice treated with only single-agent ICB, again obtaining tissue at day 14, 5 days after initiation of ICB. In the dLN, Ki67 staining of T-bet$^+$CD4$^+$ T cells appeared to correlate with the degree of antitumor activity. Combination ICB induced the biggest change, followed by αCTLA-4 monotherapy and then αPD-1 monotherapy, the later not reaching statistical significance (Supplemental Figure 5C). The same trend was also observed when evaluating the proportion of CD62L$^+$CD44$^–$ and CD62L$^–$CD44$^+$T-bet$^+$CD4$^+$ T cells in the dLN (Supplemental Figure 5D). In the TILs, increases in T cell numbers were not detected after single-agent ICB, nor did we detect quantitative changes in any CD4$^+$ T cell subset (Supplemental Figure 5, G and H). We suspect that our inability to detect any T cell changes in the TILs simply reflects the limitations of the sensitivity of our analysis and perhaps kinetic factors. The synergistic effects of combination treatment on quantifiable changes in T cells is similar to what has been described in the MB49 model (16).

Determining the role of tumor cell expression of MHC I/II and Ifngr1 in ICB response. We next tested the possibility that antitumor activity mediated by CD4$^+$ T cells relied on direct engagement of MHC class II on tumor cells or activation of IFN-γ receptor (Ifngr1) by secreted IFN-γ. We also sought to generate further evidence that direct engagement of MHC class I by CD8$^+$ T cells is not necessary for tumor rejection in this model. In vivo, MCB6C tumor cells express cell surface MHC class I (H-2Kb and H-2Db) and MHC class II (I-Ab) as well as PD-L1 (Figure 4A). We used CRISPR/Cas9 to eliminate MHC class II or Infgr1 in MCB6C. We also used CRISPR/Cas9 to target β2 microglobulin (*B2m*), a component of the MHC class I receptor complex necessary for cell surface expression of both class I proteins. For all 3 targets, MCB6C was transfected with a Cas9-expressing vector and an appropriate gRNA. Two unique subclones with homozygous disruption of the target alleles were then identified. B2m-KO clones displayed loss of B2m protein expression by Western blot (Figure 4B). Ifngr1-KO clones showed loss of expression of Ifngr1, as shown by flow cytometry (Figure 4C). MHC class II–KO clones showed loss of cell surface MHC class II expression despite IFN-γ treatment (Figure 4D). We further confirmed lack of cell surface MHC class I on B2m-KO clones after IFN-γ exposure (Figure 4E). Ifngr1-KO clones did not upregulate MHC class I, MHC class II, or PD-L1 in response to IFN-γ treatment (Figure 4F), confirming these cells lack functional Infgr1.

KO subclones were then used to establish in vivo tumors. In all cases, the KO clones showed similar growth kinetics compared with mice bearing the parental MCB6C line, which was injected in parallel (Figure 4G). We then tested the activity of combination checkpoint blockade against the various clonal lines. Five mice were injected with each line and, invariably, combination checkpoint blockade led to complete rejection, establishing that none of targets are necessary for ICB activity (Figure 4G). Flow cytometric analysis of in vivo tumors generated with Ifngr1-KO clones demonstrated that they lacked expression of

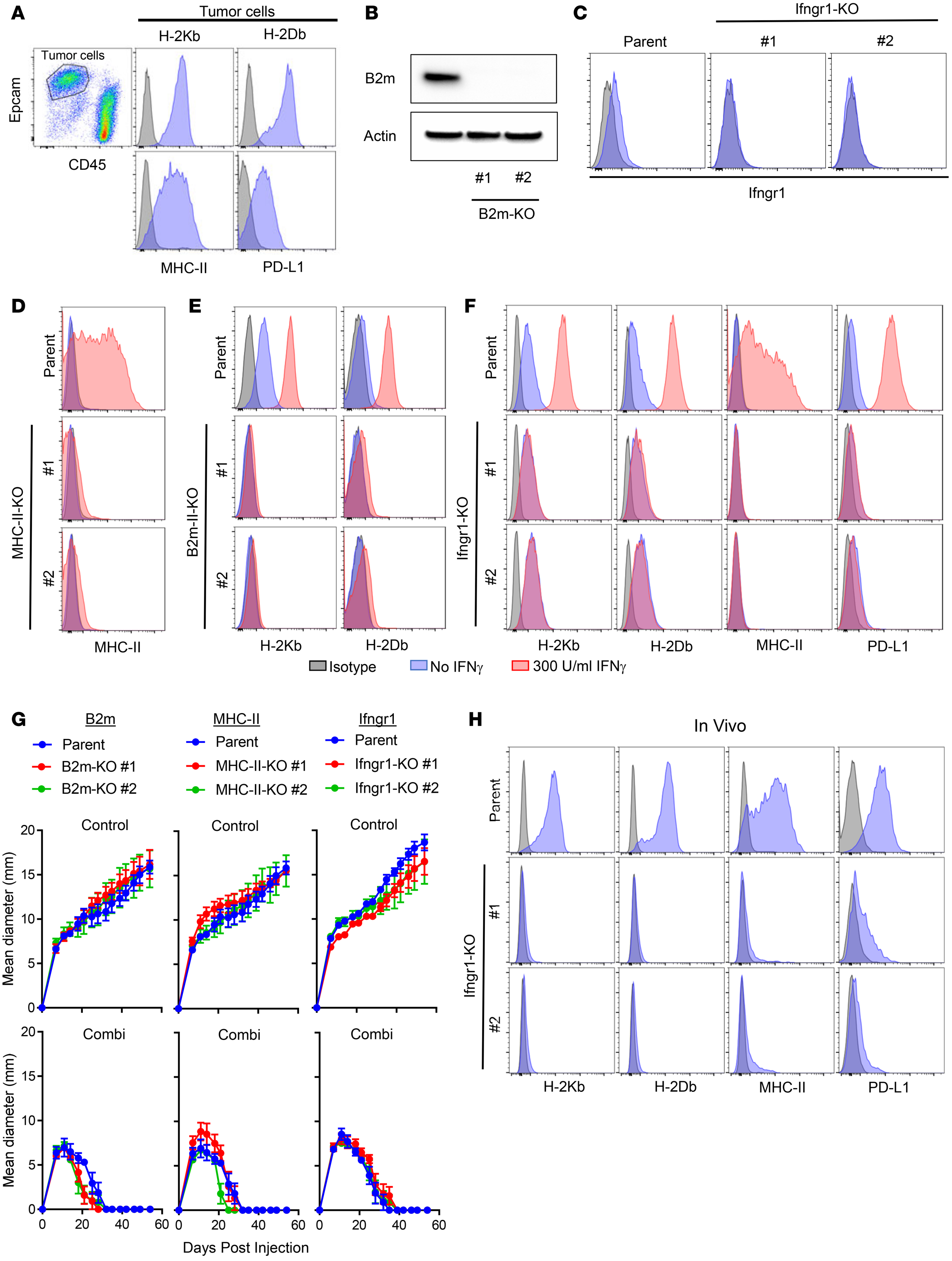
A
Tumor cells
H-2Kb
H-2Db
Tumor cells
Epcam
CD45
MHC-II
PD-L1
B
B2m
Actin
#1
#2
B2m-KO
C
Ifngr1-KO
Parent
#1
#2
Ifngr1
D
Parent
MHC-II-KO
#1
#2
MHC-II
E
Parent
B2m-II-KO
#1
#2
H-2Kb
H-2Db
F
Parent
Ifngr1-KO
#1
#2
H-2Kb
H-2Db
MHC-II
PD-L1
Isotype
No IFNγ
300 U/ml IFNγ
G
B2m
Parent
B2m-KO #1
B2m-KO #2
MHC-II
Parent
MHC-II-KO #1
MHC-II-KO #2
Ifngr1
Parent
Ifngr1-KO #1
Ifngr1-KO #2
Control
Combi
Mean diameter (mm)
0
5
10
15
20
0
20
40
60
Days Post Injection
H
In Vivo
Parent
Ifngr1-KO
#1
#2
H-2Kb
H-2Db
MHC-II
PD-L1

Figure 4. Immune checkpoint blockade–induced rejection of MCB6C tumors is not dependent on expression of MHC I/II or Infgr1 on tumor cells. (**A**) In vivo MHC class I, MHC class II, and PD-L1 expression on MCB6C tumor cells 14 days after injection. (**B**) B2m expression, as shown by Western blot, of MCB6C using B2m-KO clones grown in vitro. (**C**) Flow cytometric evaluation of Ifngr1 expression on MCB6C Ifngr1-KO clones in vitro. (**D**) Flow cytometric evaluation of MHC II on MCB6C MHC II–KO clones in vitro, with and without IFN-γ stimulation. (**E**) Flow cytometric evaluation of MHC I on MCB6C B2m-KO clones in vitro, with and without IFN-γ stimulation. (**F**) Flow cytometric evaluation of MHC I, MHC II, and PD-L1 on MCB6C Ifngr1-KO clones in vitro, with and without IFN-γ stimulation. (**G**) In vivo tumor growth of B2m-, MHC II–, or Ifngr1-KO MCB6C lines with and without combination ICB starting 9 days after tumor injection. Data are shown as mean ± SEM. *n* = 5 per organoid line per treatment. (**H**) Flow cytometric evaluation of MHC I, MHC II, and PD-L1 on MCB6C Ifngr1-KO clones from MCB6C tumor cells grown in vivo and harvested on day 11.

MHC class I and MHC class II and had relative downregulation of PD-L1, indicating that IFN-γ in the tumor microenvironment is the primary driver of their expression (Figure 4H). These findings also argue against the possibility that a redundant function of MHC class I and MHC class II explains the activity of ICB in the single-KO clones. Thus, neither direct engagement of MHC class I/II on tumor cells nor direct activation of Infgr1 explains the activity of ICB in MCB6C tumors.

Determining if IFN-γ mediates ICB response. To better understand how ICB induces tumor killing, we evaluated tumor sections obtained 5 days after ICB initiation. Compared with control tumors, treated tumors showed markedly altered tumor histology. Both the epithelial and stromal compartments were already dramatically infiltrated and disrupted by inflammatory cells within 5 days (Supplemental Figure 6A). Additionally, we identified numerous multinucleated giant cells in ICB-treated tumors consistent with a type IV hypersensitivity reaction (Supplemental Figure 6B). While our prior data refuted a role for IFN-γ in directly killing tumor cells, IFN-γ has established roles in other cell types within the tumor microenvironment, including endothelial cells, myeloid cells, and fibroblasts. Therefore, we reasoned that IFN-γ may still be necessary for ICB-mediated tumor rejection. To test this, we again treated MCB6C tumor–bearing mice with combination ICB every 3 days from day 9–24, this time also coadministering IFN-γ–neutralizing antibodies every 3 days, from day 8–23. As expected, combination ICB induced significant tumor regression (Figure 5A). The addition of IFN-γ neutralization to ICB significantly diminished the activity of ICB. Furthermore, comparing tumor sizes between the IFN-γ–neutralizing antibody alone group and the IFN-γ–neutralizing antibody plus ICB group did not reveal a statistically significant difference.

To gain further evidence supporting a key role of IFN-γ in tumor rejection, we took advantage of the observation that Ck5$^+$ epithelial tumor cells are largely eliminated by 5 days after ICB treatment. We again treated MCB6C tumor-bearing mice with combination ICB on days 9 and 12, with or without coadministration of IFN-γ–neutralizing antibodies on days 8 and 11. The effects on tumor histology 5 days after ICB initiation were then assessed using tumors from 9 distinct mice from each treatment group. Four ×20 fields from each tumor were used to determine an average percentage area of Ck5$^+$ staining, as a surrogate of viability of the epithelial compartment. The mean from each of the 9 tumors was then plotted and compared. As expected, Ck5$^+$ cells were significantly depleted by combination ICB, and IFN-γ neutralization again significantly impaired the activity of ICB (Figure 5, B and C). We used a similar approach to also evaluate the role of TNF-α, using TNF-α–neutralizing antibodies, but did not observe any reduction in ICB activity (Supplemental Figure 7A).

These data suggested that IFN-γ is the primary mediator of ICB activity in this system. To test the antitumor activity of IFN-γ directly, we engineered MCB6C to express recombinant mouse IFN-γ, utilizing an Infgr1-KO MCB6C subline so that we could determine if IFN-γ expression restricts in vivo tumor growth, independent of direct activity in the epithelial compartment. Furthermore, these experiments were carried out in mice following CD4$^+$ T cell depletion to evaluate if IFN-γ mediates antitumor activity independent of other CD4$^+$ T cell functions. We stably introduced a doxycycline-regulated vector that expresses IFN-γ as a polypeptide with dsRED (separated by a protease cleavage site), such that dsRED serves a direct marker of IFN-γ production. Consistent with the tendency of inducible vectors to have leaky expression in vivo, we observed constitutive expression of recombinant IFN-γ in the MCB6C stable sublines, and the administration of doxycycline via chow further increased expression (Supplemental Figure 7B). Over a 34-day experiment in CD4$^+$ T cell–depleted mice, the MCB6C parent line attained a mean diameter of approximately 15 mm (Figure 2A). In contrast, the constitutively expressing IFN-γ organoids grew poorly, despite CD4$^+$ T cell depletion prior to organoid injection, achieving a mean diameter of approximately 5 mm (Figure 5D). To confirm that the poor organoid growth was mediated by IFN-γ, we also coinjected either control or IFN-γ–neutralizing antibodies. IFN-γ neutralization strongly enhanced growth, as determined by tumor measurements and by tumor weight at the endpoint of the experiment (Figure 5, D and E). Thus,

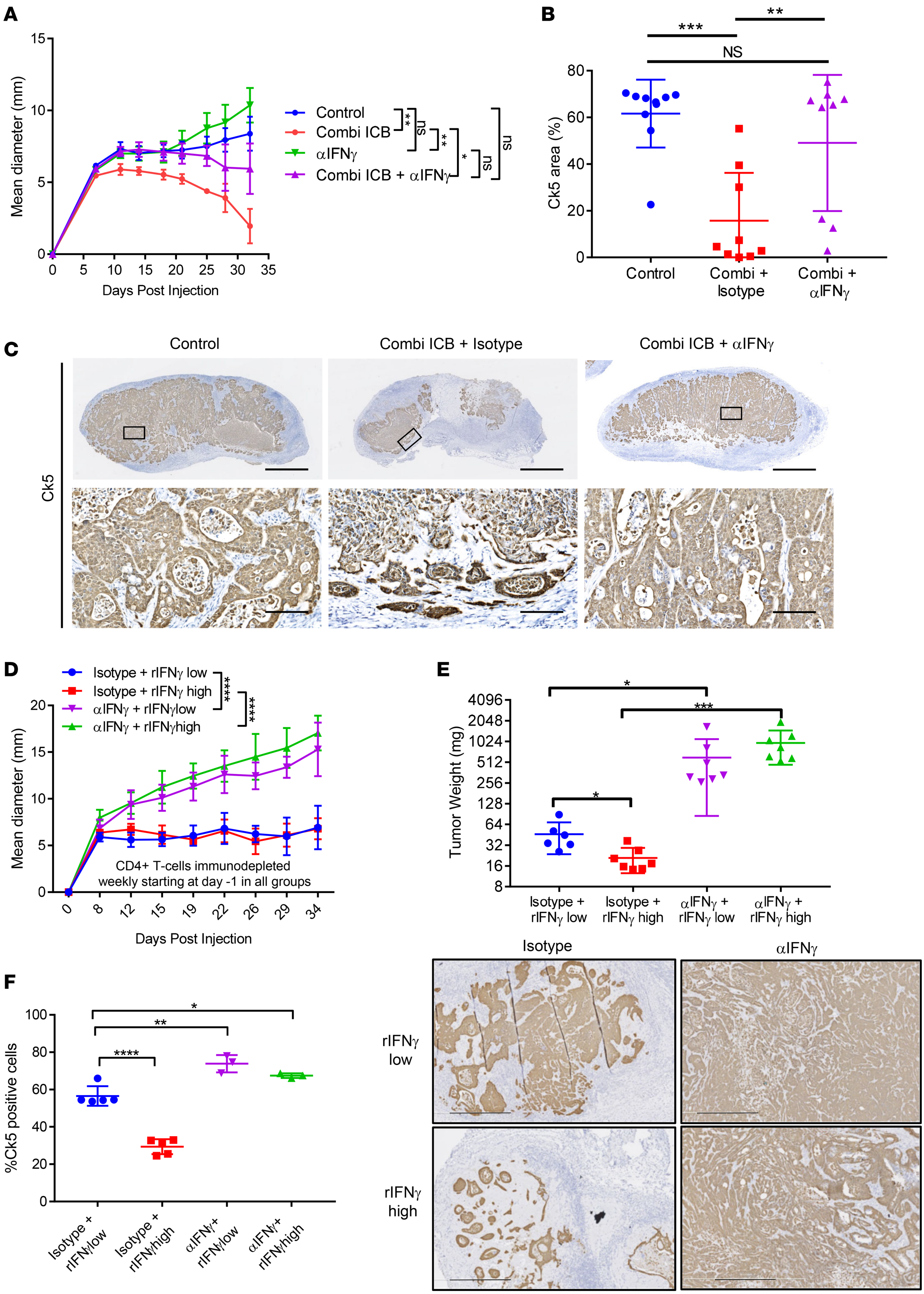
A
Mean diameter (mm)
Days Post Injection
Control
Combi ICB
αIFNγ
Combi ICB + αIFNγ
**
ns
**
*
ns
ns
B
Ck5 area (%)
***
**
NS
Control
Combi + Isotype
Combi + αIFNγ
C
Control
Combi ICB + Isotype
Combi ICB + αIFNγ
Ck5
D
Isotype + rIFNγ low
Isotype + rIFNγ high
αIFNγ + rIFNγlow
αIFNγ + rIFNγhigh
****
****
Mean diameter (mm)
CD4+ T-cells immunodepleted weekly starting at day -1 in all groups
Days Post Injection
E
Tumor Weight (mg)
*
***
*
Isotype + rIFNγ low
Isotype + rIFNγ high
αIFNγ + rIFNγ low
αIFNγ + rIFNγ high
F
%Ck5 positive cells
*
**
****
Isotype + rIFNγlow
Isotype + rIFNγhigh
αIFNγ+ rIFNγlow
αIFNγ+ rIFNγhigh
Isotype
αIFNγ
rIFNγ low
rIFNγ high

Figure 5. IFN-γ mediates ICB activity and is sufficient to inhibit tumor growth. (**A**) αPD-1 and αCTLA-4 combination treatment from day 9 to 24 coadministered with IFN-γ–neutralizing antibodies administered i.p. every 3 days from day 8 to 23. Tumor sizes were compared for an additional 9 days after the last IFN-γ neutralization, a time frame within the reported half-life of the neutralizing antibody. Data represent mean tumor diameter ± SEM. *n* = 5 per group. (**B**) Quantification of Ck5 staining of MCB6C tumor sections obtained 5 days after initiation of combination ICB with and without IFN-γ neutralization. IFN-γ neutralization antibody was administered on days 8 and 11 after MCB6C injection. Quantification was performed using images at an original magnification of ×20. For each tumor, percentage Ck5 positivity was averaged from 4 independent fields and quantified using ImageJ software. The graph shows mean ± SD of 9 individual tumors from each treatment group. (**C**) Representative images used for **B** at low and high magnification. Scale bars: 1 mm (top); 200 μM (bottom). (**D**) MCB6C Infgr1-KO organoids constitutively expressing recombinant IFN-γ (rIFN-γ) were injected to mice. For all groups, mice were subjected to $CD4^+$ T cell depletion that was started at day –1 and continued weekly throughout the duration of the experiment. IFN-γ neutralization or control treatments were also started at day –1 and continued weekly for the duration of the experiment. The low IFN-γ group was maintained on regular chow. The high IFN-γ group was initiated on doxycycline-containing chow at day 8. Constitutive low and high ectopic IFN-γ expression in tumor epithelial cells was confirmed by flow cytometry (see Supplemental Figure 7B). Data are plotted as mean ± SEM of *n* = 6–7 mice per group. (**E**) Mass of tumors described in **D** at day 34. (**F**) Ck5 staining and quantification as described in **B**. Representative images used for Ck5 quantification. Scale bars: 500 μM. Three tumors from each IFN-γ neutralization groups were scored for Ck5 positivity, and the remainder were utilized for flow cytometric analysis (See Supplemental Figure 7B). Comparisons for growth curves are by 2-way ANOVA for repeated measures and for column data are by Student's *t* test. NS > 0.05, $*P < 0.05$, $**P < 0.01$, $***P < 0.001$, $****P < 0.0001$.

IFN-γ impairs tumor growth, independent of direct activation of Ifngr1 in tumor cells and independent of other $CD4^+$ T cell functions.

In addition, some of the mice were initiated on doxycycline treatment starting at day 8 after organoid injection, so that we could determine if the IFN-γ dose in the tumor microenvironment affects tumor growth. In the absence of IFN-γ neutralization, tumors were small regardless of doxycycline exposure, and no clear difference was discernible based on caliper measurements. However, at the endpoint of the experiment, the average tumor weight in the high IFN-γ group (plus doxycycline) was significantly less than that in the low IFN-γ group (no doxycycline) (Figure 5E). We further evaluated Ck5 staining and found that the addition of doxycycline led to a striking decrease in the proportion of the tumor mass comprising epithelial tumor cells, with only scant presence of epithelial cells throughout the small mass (Figure 5F). Multiplying total tumor mass by percentage of Ck5 positivity, we estimated the mass of the epithelial compartment and found a large (~6-fold) and statistically significant difference between the high and low IFN-γ groups (Supplemental Figure 7C). Thus, introducing higher levels of ectopically expressed IFN-γ in the tumor microenvironment is sufficient to reduce epithelial tumor cell mass. In contrast to ICB, however, ectopic IFN-γ expression did not lead to complete tumor rejection. Perhaps the simplest explanation for this discrepancy is that, since the tumor cells themselves are the source of IFN-γ production in these experiments, the concentration of IFN-γ becomes insufficient for antitumor activity as the epithelial cell density diminishes, generating an equilibrium dynamic. In contrast T cells activated by ICB continue to produce IFN-γ even as the tumor cells themselves are killed. While we cannot formally exclude that other factors may a play a role in complete tumor rejection that we observe with ICB, these data confirm a principle antitumor role for IFN-γ, even in the absence of Infgr1 in the epithelial compartment.

Discussion

Mechanism of ICB antitumor activity in MCB6C. Our data show that ICB can induce expansion of T-bet^+CD4^+ T cells and complete rejection of established tumors by a $CD4^+$ T cell–dependent mechanism, even after $CD8^+$ T cell depletion or MHC class I elimination on tumor cells. The MCB6 tumors have a high overall mutation burden and presumably can release neoantigens to be taken up by antigen-presenting cells in the tumor microenvironment, stimulating $CD4^+$ T cells (Figure 6). To our knowledge, this is the first documentation of a $CD8^+$ T cell–independent mechanism of $CD4^+$ T cell–dependent tumor killing induced by ICB. A distinguishing feature of our work that may contribute to our findings is the use of organoid-culturing approaches to propagate tumor cells. In vitro organoids maintain the genetic and molecular features of the parent tumor with high fidelity and, when implanted in vivo, generate an organized microenvironment reminiscent of the primary tumor (28–30). By extension, organoid cultures would be expected to preserve the antigenic profile of the parent tumor. If tumor cells harboring the most potent class I antigens were selected against during in vivo tumorigenesis, perseveration of that antigenic profile could be one reason we did not observe strong MHC class I antigen-driven responses. It is not yet established if organoid approaches retain with high fidelity other phenotypes of relevance to tumor immunity, but co-clinical trials support the notion that organoid xenograft responses parallel drug responses observed in the patient from which they

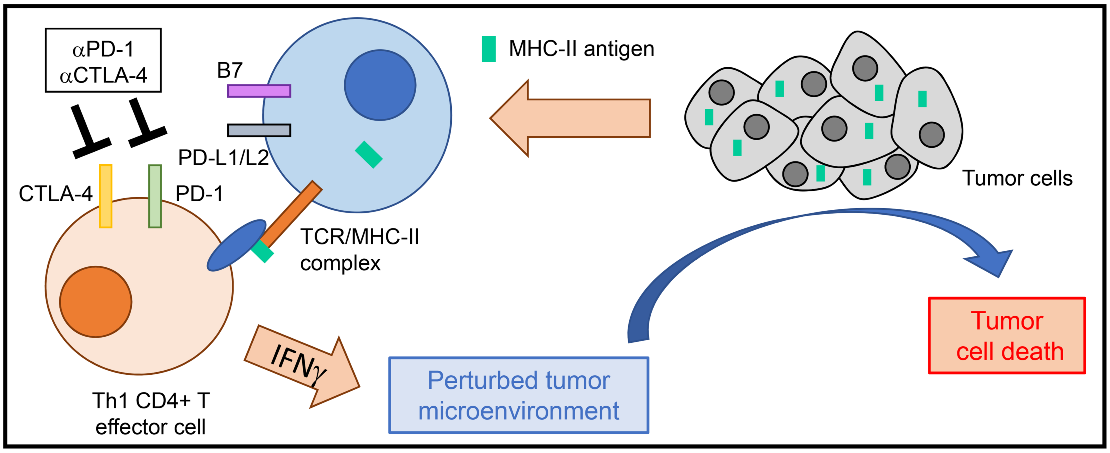

Figure 6. Schematic of ICB activity in MCB6C model. Th1 CD4$^+$ T cells increase after combination ICB and release IFN-γ, which perturbs the tumor microenvironment. ICB activity does not require MHC II expression on tumor cells, so it is presumed in this model that Th1 CD4$^+$ T cells are stimulated within the tumor microenvironment by antigen-presenting cells that have taken up tumor antigens.

were derived, even when the drug targets aspects of the microenvironment, such as angiogenesis (31). Thus, syngeneic organoid-based tumors may also be a promising tool for modeling responses to immune therapy.

In the organoid tumors, we identified IFN-γ as the principle mediator of ICB antitumor activity. While IFN-γ has previously been associated with ICB activity, this is to our knowledge the first direct demonstration that its antitumor activities are not limited to the epithelial compartment after ICB. These findings are consistent with older studies that established in tumor vaccine models that CD4$^+$ T cells can induce IFN-γ–dependent tumor immunity through indirect mechanisms (32). One important target of IFN-γ for CD4$^+$ T cell–dependent antitumor activity that has been defined in vaccine models is endothelial cells in the tumor microenvironment (33–35). It is also reasonable to speculate that IFN-γ released from CD4$^+$ T cells may affect myeloid cell function, perhaps activating macrophage tumoricidal activity, which has long been appreciated in vitro (36). Our finding that CD4$^+$ T cells are primarily located in the stromal region is consistent with a model in which they are stimulated and exert their effector function outside of the epithelial compartment. While we did not observe clear histologic changes by IHC analysis in CD31$^+$ endothelial cells following ICB (Supplemental Figure 6C) nor did we observe a quantitative difference in the representation of any myeloid lineages by flow cytometry (Supplemental Figure 8), future studies that evaluate the effects of ICB on endothelial cell, myeloid cell, and fibroblast cell function will need to be undertaken as a part of efforts to dissect the ultimate mechanisms of tumor killing.

Clinical correlation and implications. Our findings are compatible with the limited characterization to date of clinical responses to ICB in bladder cancer patients. In particular, an IFN-γ response signature correlated with bladder cancer response to PD-1 blockade, and αCTLA-4 therapy lead to expansion of IFN-γ–producing CD4$^+$ T cells (7, 15). Our data further align with analysis of ICB activity in other solid tumor types. In an integrated evaluation of clinical trials testing the PD-1 inhibitor pembrolizumab, IFN-γ signatures in pretreatment samples consistently correlated with clinical response (11). Mass cytometry performed on melanoma samples showed that, compared with normal donor blood, CTLA-4 blockade with ipilimumab lead to expansion of intratumoral CD4$^+$ T cells with a Th1-like phenotype characterized by expression of T-bet, and expansion of this cell population correlated with clinical benefit (14, 27). In a neoadjuvant head and neck cancer trial, analysis of surgical specimens from 23 patients obtained 2–3 weeks after a single dose of the PD-1 inhibitor pembrolizumab revealed that, even within this short time period, 43% of patients had evidence of a pathologic treatment response characterized by tumor necrosis and/or the presence of an inflammatory infiltrate, including giant cells, suggesting parallels to the acute histologic effects we observed after ICB (37). In potential conflict with our findings, however, melanoma and lung cancer patients with acquired resistance to PD-1 blockade have been found to have acquired loss of function of B2M consistent with an important role of CD8$^+$ T cells (38, 39). The identification of such mutations in association with resistance remains rare, and another study reported that a melanoma patient partially responded to the PD-1 inhibitor nivolumab, despite a frameshift mutation in B2M and loss of heterozygosity (40).

It is, thus, likely that more than one mechanism of ICB-mediated tumor rejection is of clinical relevance. Tissue of origin, molecular features, and disease sites may all potentially determine the relevant mechanisms in an individual patient. For biomarker discovery efforts, our work supports detailed evaluation of the tumor microenvironment, with a focus on CD4$^+$ T cells that may not necessarily be localized within the epithelial compartment. Our work should also foster broader conceptualization of how to best augment ICB activity. General strategies to activate CD4$^+$ and CD8$^+$ T cells overlap, but there may be features of CD4$^+$ T cell activation and tumor killing that can be specifically cotargeted. For example, Kreiter et al. used tumor sequencing and bioinformatic approaches to develop MHC class II antigen vaccines sufficient to induce CD4$^+$ T cell–dependent therapeutic antitumor immunity (41). In the case of localized UC, related approaches may already be underway in the clinic, as PD-1 and PD-L1 blockade are actively being tested in combination with BCG, which has proven antitumor activity against UC and is a classical activator of a type IV hypersensitivity response (Clinicaltrials.gov, NCT02792192, NCT03345134). While speculative, augmenting indirect tumor killing may ultimately contribute to the best clinical efficacy, since such a mechanism may not require ubiquitous expression of immunogenic antigens throughout a tumor mass in order to achieve a complete response.

Methods

Mice. Five- to six-week-old male C57BL/6 male mice were purchased from Taconic Farms for all experiments. Organoids were injected when the mice were 6–8 weeks old.

Mouse bladder organoid generation and culturing. To generate MCB6A and MCB6C, mice were treated with BBN 0.1% via drinking water for 22 weeks. Urothelium was then dissected from a tumor-bearing bladder, minced into smaller pieces with scissors, digested with collagenase type II (17101015, Gibco), and then resuspended at 5 mg/ml in Advanced DMEM/F12+++ medium (advanced DMEM/F-12 medium [12634028, Gibco] supplemented with 1% penicillin-streptomycin and 1% HEPES [MT25060CI, Corning]), 5 μM ROCK1/2 inhibitor Y-27632 (72302, Stemcell Technologies), and 0.2 mg/ml elastase (E7885, MilliporeSigma) for 4 hours at 37°C while shaking at 700 rpm. Cells were then pelleted at 500 *g* for 5 minutes and digested with TrypLE (12605010, Gibco) for 30 minutes at 37°C with shaking at 700 rpm. Cells were washed with Advanced DMEM/F12+++ medium and resuspended in growth factor reduced Matrigel (356231, Corning) at 10,000 cells per a 50 μl Matrigel tab. Tabs were incubated at 37°C for 15 minutes to allow Matrigel to harden. Once hardened, tabs were cultured in organoid medium prepared as described previously (28), except for the following changes: the final concentration of EGF was 5 ng/μl, the final concentration of A83-01 was 20 nM, and FGF10, FGF2, dihydrotestosterone, Y- 27632, SB202190, and primocin were omitted. Organoids were split approximately every 7 days. A polyclonal organoid line (MCB6) was generated from a tumor-bearing bladder, and, subsequently, single organoids were isolated to generate MCB6A and MCB6C. Organoid cultures are confirmed to be negative for mycoplasma.

In vivo tumor experiments. Organoids were harvested and treated with TrypLE (12605010, Gibco) to generate a single-cell suspension. One million organoid cells resuspended in 1:1 PBS/growth factor–reduced Matrigel (Corning) were injected s.c. into the right flank of the mouse. Tumor growth was monitored at least 2 times a week using digital calipers. The mean of long and short diameters was used for tumor growth curves. Mice were euthanized when tumors were >2 cm or severely ulcerated. For treatment studies, cages of 5 mice were arbitrarily assigned to a treatment group. The measurer of tumor size was not blinded to the treatment group. For ICB studies, mice were injected with 250 μg/mouse αPD-1 (RMP1-14, BioXcell) and/or 200 μg/mouse αCTLA-4 (9D9, BioXcell) i.p. every 3 days from day 9 after organoid implantation through day 24. 250 μg/mouse rat IgG2a (2A3, BioLegend) and 200 μg/mouse IgG2b (MPC-11, BioXcell) were used as isotype controls. For T cell depletion, 250 μg/mouse αCD4 (GK1.5, BioXcell) and/or 250 μg/mouse αCD8β (53-5.8, BioXcell) were injected i.p. weekly, as described in figure legends. For NK depletion, 200 μg/mouse αNK1.1 (PK136, BioXcell) was injected i.p. every 4 days (days 7, 11, 15, 19, 23, and 27). For IFN-γ–neutralizing experiments, 250 μg/mouse isotype (PIP, Leinco Technologies) or anti–IFN-γ (H22, Leinco Technologies) antibodies were i.p. injected, as described in figure legends. For TNF-α neutralization, TN3-19.12 (250 μg i.p.) was administered on days 8 and 11. Distinct epitopes were targeted by flow cytometry to confirm depletion. For CD4$^+$ T cell depletion studies, clone GK1.5 and RM4-4 were used for depletion and flow detection, respectively. For NK cell depletion studies, NK1.1 and CD335 (NKp46) were used for depletion and detection, respectively. For CD8$^+$ depletion studies, CD8β was depleted with 53-5.8 and CD8 depletion was confirmed by flow cytometry using anti-CD8α antibody (clone 53-6.7).

Generation of IFN-γ–expressing MCB6C organoids. The mouse IFN-γ ORF was purchased from Gene Script (OMu18252C) and subcloned into cloned into pCW-FLAG-2A-DSRED vector by In-fusion (Clonetech). The vector was verified by sequencing and then introduced into MCB6C Infgr1 KO #1 using LipoD293 (Signagen Laboratories). Stably transfected clones were selected by 2 weeks of puromycin exposure. Organoids were treated with doxycycline in vitro, and dsRED-expressing subclones were isolated and expanded. IFN-γ expression in vitro was further verified by ELISA. 625 ppm doxycycline-containing chow was fed to mice to induce high expression. Expression of the vector was expressed by flow cytometry for dsRED expression in EpCam CD45$^-$ cells from disassociated tumors.

RNA-seq and genomic analysis. MCB6C, MCB6A, and MCU24 cell lines were seeded in biological triplicate in 12-well tissue culture plates. Fourteen days later, RNA was isolated with the RNeasy Mini Kit (74106, Qiagen). RNA library prep and sequencing were done by the Genome Technology Access Center in the Department of Genetics at the Washington University School of Medicine. Library preparation was performed with 10 μg total RNA, integrity was determined by a Agilent Bioanalyzer. mRNA was isolated by poly-A selection using Oligo-dT beads (mRNA Direct kit, Life Technologies). mRNA was then fragmented in buffer containing 40 mM Tris Acetate, pH 8.2, 100 mM potassium acetate, and 30 mM magnesium acetate at 94 degrees for 150 seconds. mRNA was reverse transcribed to yield cDNA using SuperScript III RT enzyme (Life Technologies) and random hexamers. A second-strand reaction was performed to yield ds-cDNA. cDNA was blunt ended, had an A base added to the 3′ ends, and then had Illumina sequencing adapters ligated to the ends. Ligated fragments were then amplified using primers incorporating unique index tags. Fragments were sequenced on an Illumina HiSeq-3000 using single reads extending 50 bases. RNA-seq reads were aligned to the Ensembl release 76 top-level assembly with STAR version 2.0.4b. Gene counts were derived from the number of uniquely aligned unambiguous reads by Subread:featureCount version 1.4.5. Transcript counts were produced by Sailfish version 0.6.3. Sequencing performance was assessed for the total number of aligned reads, total number of uniquely aligned reads, genes and transcripts detected, ribosomal fraction known junction saturation, and read distribution over known gene models with RSeQC version 2.3.

Mutation calling. BAM files from RNA-seq analysis obtained in triplicate from MCB6C or MCU24 were merged into one single file for each organoid line. To determine variation against the reference at the base level, read sequence were lined up using samtools mpileup (42). Variants were then called using VarScan version 2.3.9 using a minimum coverage cutoff of ×10. Default values were used for the remaining parameters with the exceptions of (a) minimum number of supporting reads at a location in order to call a variant, which was set to 4, and (b) minimum minor variant allele frequency, which was set to 0.05 (43). Any corresponding mutations detected in the normal organoid line, MCU24, were considered to represent probable germ-line variants and were removed. Variant calls identified in MCB6C were then annotated using GATK tools version 3.8-0-ge9d806836 by mapping them to the mouse dbSNP database (44). Potential functional consequences of identified mutations were assessed by determining whether they occurred within functional units (e.g., genes, UTRs, etc.) using snpEff version 4.3T and by comparison to genes identified by Kandoth et al. in pan-cancer and bladder cancer (45, 46).

Antibodies. The following antibodies were used for flow cytometry: CD45 (30F-11, BioLegend), CD4 (RM4-4, BioLegend), CD8α (53-6.7, BioLegend), CD8β (YTS156.7.7, BioLegend), CD11b (M1/70, BioLegend), CD11c (N418, BioLegend), CD326 (EpCam, BioLegend, 118207), CD24 (M1/69, BioLegend), CD44 (IM7, BioLegend), CD62L (MEL-14, BioLegend), CD103 (2E7, eBioscience), CD206 (C068C2, BioLegend), F4/80 (BM8, BioLegend), I-A/I-E (M5/114.152, BioLegend), Ly6C (HK1.4, BioLegend), Ly6G (1A8, BioLegend), Siglec-F (E50-2440, BD Biosciences), TCRβ (H57-597, BioLegend), CD335 (NKp46, BioLegend), Foxp3 (FJK-16s, eBioscience), T-bet (4B10, BioLegend), Gata3 (TWAJ, eBioscience), RorγT (B2D, eBioscience), IFN-γ (XMG1.2, BioLegend), Ki67 (B56, BD Biosciences), H-2Kb (AF6-88.5, BioLegend), H-2Db (KH95, BioLegend), PD-L1 (10F.9G2, BioLegend), and IFN-γRα (2E2, BioLegend). For immunohistochemistry, the following antibodies were used: Ck5 (EP1601Y, Abcam), CD4 (4SM95, eBioscience), CD8α (4SM15, eBioscience), CD31 (D8V9E, Cell Signaling Technology), and NG2 (AB5320, MilliporeSigma). For Western blot, we used β2 Microgloublin (EP2978Y, Abcam).

Flow cytometry. To analyze tumor cells and immune cells, tumors were isolated, cut into small pieces, and digested for 1 hour in RPMI 1640 media containing 100 μg/ml Collagenase type IA (MilliporeSigma) and 50 U/ml of DNase I (Worthington Biochemical). Cells were washed in 2% FCS in HBSS (Corning) and filtered over 100-μm nylon mesh. After red blood cell lysis with red blood cell lysing solution (BD Bioscience), Fc-receptors were blocked with FcR-blocking reagent (Miltenyi Biotech). For cell surface staining, cells were incubated with fluorescent-conjugated antibodies, followed by incubation with 100 ng/ml DAPI to stain dead cells. For intracellular staining, cells were stained with a Zombie NIR Fixable Viability kit (BioLegend) before FcR blocking. After cell surface marker staining, cells were fixed and permeabilized using a Foxp3 staining kit (eBioscience) and intracellularly stained with fluorescent-conjugated antibodies. Thymocytes, splenocytes, or lymphocytes from lymph nodes were used as positive controls for transcription factor staining. To detect MHC class I, MHC class II, and PD-L1 expression in MCB6C in vitro, organoids were treated with 300 U/ml murine IFN-γ (BioLegend) for 2 or 7 days with one medium change at day 4. For IFN-γRα (CD119) staining, a biotin-labeled anti–IFN-γRα antibody in combination with streptavidin-PE (BioLegend) was used. Data were acquired using BD LSRFortessa X-20 (BD biosciences) and analyzed with FlowJo (Tree Star).

IHC. Tumor tissues were fixed in 4% paraformaldehyde (Electron Microscopy Sciences) overnight. 5 μm paraffin-embedded tissue sections were mounted on slides. After deparaffinization and rehydration, sections were microwaved for 20 minutes in TE solution (10 mM Tris-HCl and 0.5 mM EDTA, pH 9.0) and incubated in 3% H_2O_2 to deactivate endogenous HRP. Slides were incubated in 5% goat serum in TBS-T (0.1% Tween20 in TBS) for 1 hour at room temperature and further blocked with the AVIDIN/BIOTIN blocking kit (VECTOR). Primary antibodies were diluted in 5% goat serum in TBS-T and incubated overnight at 4°C. After 3 washes with TBS-T, biotin-conjugated secondary antibodies were added for 1 hour. After 3 washes, the VECTASTAIN kit (VECTOR) and DAB kit (VECTOR) were further used to develop signals. Counterstaining was performed with hematoxylin. After staining, the images were captured with NanoZoomer-XR digital slice scanner (Hamamatsu Photonics). Analysis was performed using NDP.view software (Hamamatsu photonics) and Image J (version1.51, NIH).

Generation of B2m, H2-Aa1, or Ifngr1-KO MCB6C organoid lines using CRISPR/Cas9. To generate MCB6C organoid lines lacking B2m, H2-Aa1, or Ifngr1 expression, we designed the single-guide RNA (sgRNA) at CRISPRdirect (http://crispr.dbcls.jp/) in 2016. The sgRNA targeting mouse B2m (5′-TCGGCTTCCCATTCTCCGGT-3′), H2-Aa1 (5′-GGAGGTGAAGACGACATTGA-3′), or Ifngr1(5′-CTGATGCTGTCTGCGAAGGT-3′) was subcloned into the pSpCas9(BB)-2A-Puro (PX459) V2.0 (Addgene plasmid 62988). For transient transfection, tumor organoid cells were dissociated with TrypLE (Invitrogen) and then incubated with plasmid mixed with LipoD transfection reagent (SignaGen laboratories) for 4 hours at 37 degrees with rotation. Cells were then pelleted, washed, and plated. Organoids were cultured as described above, and transfected clones were then selected with 72 hours of puromycin exposure starting 48 hours after transfection. Two weeks after transfection, single organoid clones were isolated and further expanded. Genomic DNA from each organoid clone was used to amplify each target genomic locus with the following primers: B2m, forward primer, 5′-GGGAAGTCTAGGGAGGAGCA-3′, reverse primer, 5′-ATGCTTAACTCTGCAGGCGT-3′; H2-Aa1, forward primer, 5′-CAGTGCAGCCCAGACAGTTA-3′, reverse primer, 5′-GTGGATTGTGAGCTGACCA-3′; and Ifngr1, forward primer, 5′-GTATTGGTCCCGCCTCTCTG-3′, reverse primer, 5′-ACACACAATGCCAAACGCTG-3′. Each PCR product was inserted into pCR II-TOPO vector (Invitrogen). M13 forward (–20) primer (5′-GTAAAACGACGGCCAG-3′) was used for Sanger sequencing to confirm disruption of the target locus.

In vitro T cell stimulation. For intracellular IFN-γ expression analysis in TILs, total tumor cells were isolated from tumors and stimulated with PMA (500 ng/ml), ionomycin (50 ng/ml), and GolgiPlug (BD Biosciences) for 4 hours. Cells were then washed, and viable cells were identified with the Zombie NIR Fixable Viability kit (BioLegend) before FcR blocking. After cell surface marker staining, cells were fixed and permeabilized with the Foxp3 staining kit (eBioscience). Cells were then intracellular stained and analyzed by flow cytometry.

In vitro organoid stimulation. To detect MHC class I and MHC class II expression on MCB6C organoids in vitro, MCB6C organoids cultured for 7 days were then stimulated with IFN-γ (300 U/ml, BioLegend) for 2 days (MHC class I) or 7 days (MHC class II). For MHC class II detection, media containing IFN-γ were changed once after 4 days of exposure.

Statistics. Statistical analyses were performed using Prism 7.0 (GraphPad). For all tumor growth curve comparisons, 2-way ANOVA for repeated measures was used. For all other comparisons, an unpaired Student's *t* test was used. All tests were 2-tailed. *P* values of less than 0.05 were considered significant.

Study approval. Mice were handled and housed according to protocols approved by the Washington University School of Medicine Institutional Animal Care and Use Committee.

Author contributions

YS and JKB designed and executed experiments, interpreted data, and generated figures. XS executed experiments and interpreted data. AME and CAM executed bioinformatic analysis of sequencing data. JKS reviewed histology slides. VKA designed experiments, interpreted data, generated figures, and wrote the manuscript.

Acknowledgments

We thank Russell Pachynski, Robert Schreiber, and members of the Schreiber lab for helpful comments and suggestions over the course of the study. VKA received funding for the project from Department of Defense grant W81XWH- 17-1-0562. Technical support was provided by the (a) Immunomonitoring Laboratory (IML), which is supported by the Andrew M. and Jane M. Bursky Center for Human Immunology and Immunotherapy Programs at Washington University, and the (b) Genome Technology Access Center (GTAC) in the Department of Genetics at Washington University School of Medicine. The IML and GTAC are shared resources of the Alvin J. Siteman Cancer Center and are also supported by National Cancer Institute Cancer Center Support Grant P30CA9184

Address correspondence to: Vivek K. Arora, Washington University School of Medicine, 660 S Euclid Avenue, St. Louis, Missouri 63110, USA. Phone: 314.286.1906; Email: arorav@wustl.edu.

YS's present address is: Drug Discovery & Disease Research Laboratory, Shionogi & Co. Ltd., Osaka, Japan.

---

1. Ratliff TL, Gillen D, Catalona WJ. Requirement of a thymus dependent immune response for BCG-mediated antitumor activity. *J Urol*. 1987;137(1):155–158.
2. Lamm DL, et al. A randomized trial of intravesical doxorubicin and immunotherapy with bacille Calmette-Guérin for transitional-cell carcinoma of the bladder. *N Engl J Med*. 1991;325(17):1205–1209.
3. Rosenberg JE, et al. Atezolizumab in patients with locally advanced and metastatic urothelial carcinoma who have progressed following treatment with platinum-based chemotherapy: a single-arm, multicentre, phase 2 trial. *Lancet*. 2016;387(10031):1909–1920.
4. Balar AV, et al. Atezolizumab as first-line treatment in cisplatin-ineligible patients with locally advanced and metastatic urothelial carcinoma: a single-arm, multicentre, phase 2 trial. *Lancet*. 2017;389(10064):67–76.
5. Balar AV, et al. First-line pembrolizumab in cisplatin-ineligible patients with locally advanced and unresectable or metastatic urothelial cancer (KEYNOTE-052): a multicentre, single-arm, phase 2 study. *Lancet Oncol*. 2017;18(11):1483–1492.
6. Bellmunt J, et al. Pembrolizumab as second-line therapy for advanced urothelial carcinoma. *N Engl J Med*. 2017;376(11):1015–1026.
7. Sharma P, et al. Nivolumab in metastatic urothelial carcinoma after platinum therapy (CheckMate 275): a multicentre, single-arm, phase 2 trial. *Lancet Oncol*. 2017;18(3):312–322.
8. Powles T, et al. Efficacy and safety of durvalumab in locally advanced or metastatic urothelial carcinoma: updated results from a phase 1/2 open-label study. *JAMA Oncol*. 2017;3(9):e172411.
9. Apolo AB, et al. Avelumab, an anti-programmed death-ligand 1 antibody, in patients with refractory metastatic urothelial carcinoma: results from a multicenter, phase Ib study. *J Clin Oncol*. 2017;35(19):2117–2124.
10. Sharma P, et al. Efficacy and safety of nivolumab plus ipilimumab in previously treated metastatic urothelial carcinoma: First results from the phase I/II CheckMate 032 study. *J Clin Oncol*. 2016; 4(15_suppl):4501.
11. Ayers M, et al. IFN-γ-related mRNA profile predicts clinical response to PD-1 blockade. *J Clin Invest*. 2017;127(8):2930–2940.
12. Powles T, et al. Atezolizumab (atezo) vs. chemotherapy (chemo) in platinum-treated locally advanced or metastatic urothelial carcinoma (mUC): immune biomarkers, tumor mutational burden (TMB), and clinical outcomes from the phase III IMvigor211 study. *J Clin Oncol*. 2018;36(6_suppl):409.
13. Früh K, Yang Y. Antigen presentation by MHC class I and its regulation by interferon gamma. *Curr Opin Immunol*. 1999;11(1):76–81.
14. Carthon BC, et al. Preoperative CTLA-4 blockade: tolerability and immune monitoring in the setting of a presurgical clinical trial. *Clin Cancer Res*. 2010;16(10):2861–2871.
15. Liakou CI, et al. CTLA-4 blockade increases IFNgamma-producing CD4$^+$ICOShi cells to shift the ratio of effector to regulatory T cells in cancer patients. *Proc Natl Acad Sci USA*. 2008;105(39):14987–14992.
16. Summerhayes IC, Franks LM. Effects of donor age on neoplastic transformation of adult mouse bladder epithelium in vitro. *J Natl Cancer Inst*. 1979;62(4):1017–1023.
17. Shi LZ, et al. Interdependent IL-7 and IFN-γ signalling in T-cell controls tumour eradication by combined α-CTLA-4+α-PD-1 therapy. *Nat Commun*. 2016;7:12335.
18. Vandeveer AJ, Fallon JK, Tighe R, Sabzevari H, Schlom J, Greiner JW. Systemic immunotherapy of non-muscle invasive mouse bladder cancer with avelumab, an anti-PD-L1 immune checkpoint inhibitor. *Cancer Immunol Res*. 2016;4(5):452–462.
19. Bertram JS, Craig AW. Specific induction of bladder cancer in mice by butyl-(4-hydroxybutyl)-nitrosamine and the effects of hormonal modifications on the sex difference in response. *Eur J Cancer*. 1972;8(6):587–594.
20. Halstead AM, et al. Bladder-cancer-associated mutations in RXRA activate peroxisome proliferator-activated receptors to drive urothelial proliferation. *Elife*. 2017;6.
21. Drost J, et al. Sequential cancer mutations in cultured human intestinal stem cells. *Nature*. 2015;521(7550):43–47.

22. Robertson AG, et al. Comprehensive molecular characterization of muscle-invasive bladder cancer. *Cell*. 2018;174(4):1033.
23. Kardos J, et al. Claudin-low bladder tumors are immune infiltrated and actively immune suppressed. *JCI Insight*. 2016;1(3):e85902.
24. Lee MG, et al. Demethylation of H3K27 regulates polycomb recruitment and H2A ubiquitination. *Science*. 2007;318(5849):447–450.
25. Guo G, et al. Whole-genome and whole-exome sequencing of bladder cancer identifies frequent alterations in genes involved in sister chromatid cohesion and segregation. *Nat Genet*. 2013;45(12):1459–1463.
26. Cerami E, et al. The cBio cancer genomics portal: an open platform for exploring multidimensional cancer genomics data. *Cancer Discov*. 2012;2(5):401–404.
27. Wei SC, et al. Distinct cellular mechanisms underlie anti-CTLA-4 and anti-PD-1 checkpoint blockade. *Cell*. 2017;170(6):1120–1133.e17.
28. Gao D, et al. Organoid cultures derived from patients with advanced prostate cancer. *Cell*. 2014;159(1):176–187.
29. Sachs N, Clevers H. Organoid cultures for the analysis of cancer phenotypes. *Curr Opin Genet Dev*. 2014;24:68–73.
30. Boj SF, et al. Organoid models of human and mouse ductal pancreatic cancer. *Cell*. 2015;160(1-2):324–338.
31. Vlachogiannis G, et al. Patient-derived organoids model treatment response of metastatic gastrointestinal cancers. *Science*. 2018;359(6378):920–926.
32. Mumberg D, et al. CD4(+) T cells eliminate MHC class II-negative cancer cells in vivo by indirect effects of IFN-gamma. *Proc Natl Acad Sci USA*. 1999;96(15):8633–8638.
33. Qin Z, Blankenstein T. CD4$^+$ T cell--mediated tumor rejection involves inhibition of angiogenesis that is dependent on IFN gamma receptor expression by nonhematopoietic cells. *Immunity*. 2000;12(6):677–686.
34. Beatty G, Paterson Y. IFN-gamma-dependent inhibition of tumor angiogenesis by tumor-infiltrating CD4$^+$ T cells requires tumor responsiveness to IFN-gamma. *J Immunol*. 2001;166(4):2276–2282.
35. Kammertoens T, et al. Tumour ischaemia by interferon-γ resembles physiological blood vessel regression. *Nature*. 2017;545(7652):98–102.
36. Celada A, Gray PW, Rinderknecht E, Schreiber RD. Evidence for a gamma-interferon receptor that regulates macrophage tumoricidal activity. *J Exp Med*. 1984;160(1):55–74.
37. Uppaluri R, et al. Neoadjuvant pembrolizumab in surgically resectable, locally advanced HPV negative head and neck squamous cell carcinoma (HNSCC). *J Clin Oncol*. 2017;35(15_suppl):6012.
38. Zaretsky JM, et al. Mutations associated with acquired resistance to PD-1 blockade in melanoma. *N Engl J Med*. 2016;375(9):819–829.
39. Gettinger S, et al. Impaired HLA class I antigen processing and presentation as a mechanism of acquired resistance to immune checkpoint inhibitors in lung cancer. *Cancer Discov*. 2017;7(12):1420–1435.
40. Riaz N, et al. Tumor and microenvironment evolution during immunotherapy with nivolumab. *Cell*. 2017;171(4):934–949.e16.
41. Kreiter S, et al. Mutant MHC class II epitopes drive therapeutic immune responses to cancer. *Nature*. 2015;520(7549):692–696.
42. Li H, et al. The sequence alignment/Map format and SAMtools. *Bioinformatics*. 2009;25(16):2078–2079.
43. Koboldt DC, et al. VarScan 2: somatic mutation and copy number alteration discovery in cancer by exome sequencing. *Genome Res*. 2012;22(3):568–576.
44. DePristo MA, et al. A framework for variation discovery and genotyping using next-generation DNA sequencing data. *Nat Genet*. 2011;43(5):491–498.
45. Cingolani P, et al. A program for annotating and predicting the effects of single nucleotide polymorphisms, SnpEff: SNPs in the genome of Drosophila melanogaster strain w1118; iso-2; iso-3. *Fly (Austin)*. 2012;6(2):80–92.
46. Kandoth C, et al. Mutational landscape and significance across 12 major cancer types. *Nature*. 2013;502(7471):333–339.